

See discussions, stats, and author profiles for this publication at: <https://www.researchgate.net/publication/258140537>

# A hybrid approach for modelling of plasticity and failure behaviour of advanced high-strength steel sheets

Article in *International Journal of Damage Mechanics* · March 2013

DOI: 10.1177/1056789512439319

CITATIONS

198

READS

11,519

4 authors:



**Junhe Lian**

Aalto University

154 PUBLICATIONS 1,973 CITATIONS

SEE PROFILE



**M. Sharaf**

Dassault Systèmes

13 PUBLICATIONS 299 CITATIONS

SEE PROFILE



**Fady Archie**

19 PUBLICATIONS 477 CITATIONS

SEE PROFILE



**Sebastian Muenstermann**

RWTH Aachen University

273 PUBLICATIONS 2,850 CITATIONS

SEE PROFILE

# International Journal of Damage Mechanics

<http://ijd.sagepub.com/>

---

## **A hybrid approach for modelling of plasticity and failure behaviour of advanced high-strength steel sheets**

J Lian, M Sharaf, F Archie and S Münstermann

*International Journal of Damage Mechanics* 2013 22: 188 originally published online 27 March 2012

DOI: 10.1177/1056789512439319

The online version of this article can be found at:

<http://ijd.sagepub.com/content/22/2/188>

---

Published by:



<http://www.sagepublications.com>

**Additional services and information for *International Journal of Damage Mechanics* can be found at:**

**Email Alerts:** <http://ijd.sagepub.com/cgi/alerts>

**Subscriptions:** <http://ijd.sagepub.com/subscriptions>

**Reprints:** <http://www.sagepub.com/journalsReprints.nav>

**Permissions:** <http://www.sagepub.com/journalsPermissions.nav>

**Citations:** <http://ijd.sagepub.com/content/22/2/188.refs.html>

>> [Version of Record](#) - Feb 28, 2013

[OnlineFirst Version of Record](#) - Mar 27, 2012

[What is This?](#)

# A hybrid approach for modelling of plasticity and failure behaviour of advanced high-strength steel sheets

J Lian<sup>1</sup>, M Sharaf<sup>1</sup>, F Archie<sup>2</sup> and S Münstermann<sup>1</sup>

## Abstract

The ductile damage mechanisms dominating in modern high-strength steels have emphasised the significance of the onset of damage and the subsequent damage evolution in sheet metal forming processes. This paper contributes to the modelling of the plasticity and ductile damage behaviour of a dual-phase steel sheet by proposing a new damage mechanics approach derived from the combination of different types of damage models. It addresses the influence of stress state on the plasticity behaviour and onset of damage of materials, and quantifies the microstructure degradation using a dissipation-energy-based damage evolution law. The model is implemented into ABAQUS/Explicit by means of a user material subroutine (VUMAT) and applied to the subsequent numerical simulations. A hybrid experimental and numerical approach is employed to calibrate the material parameters, and the detailed program is demonstrated. The calibrated parameters and the model are then verified by experiments at different levels, and a good agreement between the experimental and numerical results is achieved.

## Keywords

AHSS, ductile damage and fracture, damage models, crack initiation, FEM simulation

## Introduction

Driven by the demands for weight reduction and passive safety in the automotive and aerospace industry, advanced high-strength steels (AHSS) have been intensively developed and conducted in recent decades, thanks to their excellent tensile strength without the compromise of ductility. The microstructure of these steels is designed by constituents of strong distinctions in mechanical

---

<sup>1</sup>Department of Ferrous Metallurgy, RWTH Aachen University, Germany

<sup>2</sup>German University of Cairo, Egypt

### Corresponding author:

J Lian, Department of Ferrous Metallurgy, RWTH Aachen University, Germany.

Email: junhe.lian@iehk.rwth-aachen.de

properties, and this also results in new damage mechanisms. In the dual-phase steels, for example, the damage mechanism exhibits a rather complex situation: voids are generated by the debonding of the phase boundaries and the inner brittle cracking of the hard phase, as well as by inclusions and particles. Consequently, the increased possibility of creating microvoids or microcracks by the new damage mechanisms introduces the importance of the subsequent damage evolution. Tasan et al. (2009) empirically studied the correlation between the ductile damage evolution and the forming limits at various strain paths of a dual phase (DP) steel and a conventional ductile interstitial-free (IF) steel. It was shown that compared to the IF steel, an extensive damaged scale has been reached before strain localisation and a fast evolution rate has been observed in the DP steel. The study emphasised that the onset of damage rather than strain localisation becomes critical, since the microstructure degradation introduced by damage evolution could cause a qualitative change in the material strength and ductility. Therefore, a microscopic threshold that corresponds to the onset of damage should be implemented in the damage mechanics models. Furthermore, a quantitative representation to express the extent of damage is also demanded in order to guide the forming process in an industrial scale.

Damage mechanics models are basically classified into two categories, coupled and uncoupled models (Atkins, 1997; Besson, 2009). Coupled models incorporate the effect of the accumulated damage into constitutive equations. The first type, the porous plasticity model, is usually referenced to as the GTN model, initiated by the work of Gurson (1977) and further modified by Tvergaard and Needleman (Tvergaard, 1981, 1982; Tvergaard and Needleman, 1984). The formation is based on the straightforward implementation of the ductile damage mechanisms, that is, void nucleation, growth and coalescence. The void volume fraction  $f$  was introduced as the damage indicator and the damage-induced softening was taken into account in the yield potential as well as the first and second stress invariants. Further modifications (Gologanu et al., 1993, 1994, 1997; Kailasam and Castaneda, 1998; Nahshon and Hutchinson, 2008; Nielsen and Tvergaard, 2009, 2010; Xue, 2008) were introduced to improve the capability of this type of model; however, they also increase the difficulty in calibrating the parameters by more numbers than the original nine. Additionally, the identification of the large number of parameters is not direct; an iterative calibration procedure is normally employed to evaluate the mutual influence of the parameters. The prediction of the calibrated parameters on the geometries that were not involved in the calibration procedure has not been proved to be satisfactory (Bonora et al., 2005; Dunand and Mohr, 2011). In contrast, continuum damage mechanics (CDM)-based models (Kachanov, 1999; Lemaitre, 1985, 1992) treat damage evolution in a macroscopic and phenomenological way by introducing an internal variable  $D$  to quantify the microscopic material degradation. The macroscopic consideration of damage eases the formulation of the constitutive equations and the subsequent parameter calibration, but overlooks the microscopic damage mechanisms and the influence of the stress state. In addition, the damage-induced softening is assumed to take place at the same time as the plastic deformation in this type of model, while the effect of damage at this stage is not pronounced in experiments. All these limitations could lead to inaccuracy in the application of AHSS.

In contrast to the coupled models, uncoupled models define a critical loading condition responsible for the appearance of fracture. The loading condition is characterised normally by a weighted function of equivalent plastic strain, and the corresponding critical equivalent plastic strain to fracture is expressed as  $\bar{\epsilon}_f$ . It has been proved theoretically (McClintock, 1968; Rice and Tracey, 1969) and experimentally (Bao and Wierzbicki, 2004b; Hancock and Brown, 1983; Hancock and Mackenzie, 1976; Mackenzie et al., 1977; Mirza et al., 1996) that the fracture strain is strongly dependent on stress triaxiality, defined as the ratio of pressure over the equivalent stress. Recent studies have revealed that another parameter, Lode angle, related to the third invariant of the

deviatoric stress tensor, has also an unnegligible impact on the fracture strain (Bai and Wierzbicki, 2008; Barsoum and Faleskog, 2007; Gao et al., 2009a; Mirone and Corallo, 2010). These models simply provide a binary assessment: if the critical load is reached, fracture happens; otherwise, the structure is safe. The accumulated damage is uncoupled with the constitutive plasticity model. Therefore, the material deterioration is not taken into account in the material stress–strain response. Despite these limitations, the empirical models are widely adopted in many applications due to their simple formulation and ease of calibration (Li et al., 2011).

In the literature review above, the demands for modelling the damage behaviour of AHSS are raised by the new governing damage mechanisms. To address these demands, three types of ductile damage models are briefly reviewed and compared; individually, they all show certain shortcomings in representing the entire deformation process. The goal of the study is to form a consistent approach of ductile damage modelling that properly represents the new damage features of modern high-strength steel sheets. To fully cope with this aim, two terms are clearly differentiated in this study, fracture and crack initiation. Fracture describes a macroscopic behaviour that can be defined as occurring when a component or system stops complying with its service requirements. Crack initiation describes the microscopic behaviours that can be defined as occurring when the microstructure develops an irreversible degradation on a given length scale. It corresponds to a critical phase of the material degradation caused by all the microscopic discontinuities, for example, severe void coalescence and formation of microcracks or shear bands. The length scale of crack initiation is among dozens of microns, depending on the material, microstructure and loading conditions. After the crack initiation, the progressive accumulation of damage leads to the final fracture of materials. Under this concept, a hybrid approach for ductile damage modelling is formulated with three main constituents originated from pre-reviewed models, which are illustrated in Figure 1.

- A plasticity model to characterise the material behaviour before crack initiation.
- A phenomenological criterion to indicate the initiation of damage.
- A damage-induced softening part to characterise the post-damage material behaviour.

Damage or fracture is seen as a phenomenon involving large stress or strain gradients at the local potential fracture locations. To give a reliable and precise prediction of the failure in mechanical components, the accuracy of the plasticity model that delivers the local stress and strain variables is essential. In the characterisation of isotropic pressure-insensitive materials, the conventional J2 plasticity model is frequently employed, in which yielding is only dependent on the second invariant of the deviatoric stress tensor. In body-centred cubic (bcc) metals, however, the plastic flow shows the dependence on temperature, strain-rate and stress state (including a tension–compression asymmetry) due to the non-planar dislocation core structures in non-close-packed crystal lattices (Racherla and Bassani, 2007). To account for the stress–state effect on the plastic deformation, non-quadratic yield functions are formulated (e.g. Bai and Wierzbicki, 2008, 2010; Cazacu, 2004; Cazacu et al., 2006; Hershey, 1954; Hosford, 1972). Here, we employ the more generalised non-quadratic plasticity model postulated by Bai and Wierzbicki (2008), with the associated flow rule and the isotropic hardening law to characterise the stress–strain behaviour of AHSS before the crack initiation.

To indicate the moment when damage starts to play a role in the process, an empirical damage model is introduced. With a customised experimental method to measure the instant of crack initiation, the criterion here is not to indicate the final fracture ( $\bar{\epsilon}_f$ ), as it is normally adopted in the literature (Bai and Wierzbicki, 2008; Bao and Wierzbicki, 2004a; Dunand and Mohr, 2010), but to characterise the initiation of damage ( $\bar{\epsilon}_i$ ). In the void-controlled ductile damage mechanism, it

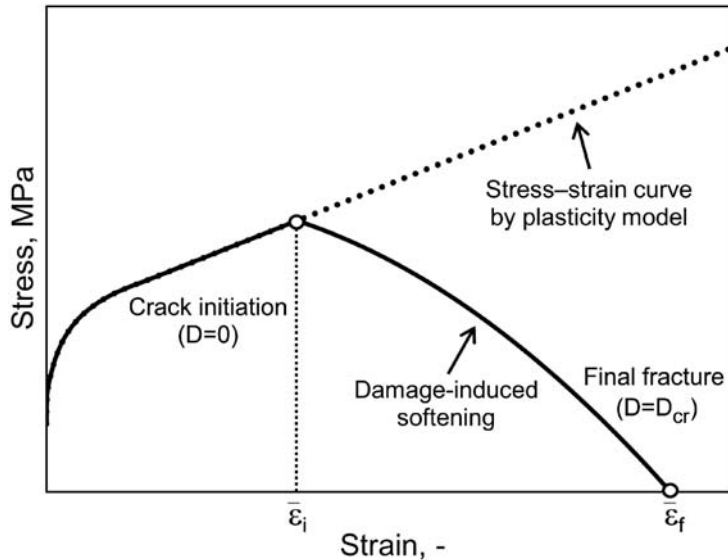


**Figure 1.** Schematic illustration of the stress–strain behaviour with the proposed approach.

physically corresponds to the critical phase of the void coalescence that leads to an accelerated damage accumulation rate, as is also emphasised in the GTN model as the critical void volume fracture,  $f_c$ . Here, the empirical ductile damage criterion postulated by Bai and Wierzbicki (2008) covering the full stress states (dependent on both stress triaxiality and Lode angle) is employed to indicate the crack initiation.

Once the  $\bar{\epsilon}_i$  is triggered at the corresponding stress state, the deformation-induced damage becomes critical until the final fracture. To represent the damage-induced softening, a damage evolution law based on the energy dissipated during the damage progress is introduced. An internal parameter  $D$  characterises the accumulated damage, and a critical value of  $D$ ,  $D_{cr}$ , represents the final separation of the continuum material, that is, fracture. With this modelling approach, the multi-scale characterisation of both damage and fracture can be realised and a quantitative representation of damage evolution can be obtained for the sheet formability prediction.

In the next section, the formulation of the framework is briefly introduced. It is followed by the experimental methodologies to identify the instant and location of the crack initiation. Subsequently, the parameter calibration procedures are defined for the three constituents of the model. Within the procedure, both the experimental program and the numerical simulation are presented. Finally, the model and calibrated parameters are validated in different levels by experiments.

## Formulation of the framework of ductile damage modelling

### Characterisation of stress state

A certain stress state,  $\underline{\sigma}$ , can be expressed by spherical and deviatoric parts

$$\underline{\sigma} = \underline{s} + p\underline{I} \quad (1)$$

where  $\underline{s}$  is the deviatoric stress tensor,  $\underline{I}$  is the identity tensor and  $p$  is the hydrostatic pressure related to the mean stress,  $\sigma_m$

$$p = -\sigma_m = -\frac{1}{3} \text{tr}[\underline{s}] \quad (2)$$

The three main invariants of the stress tensor and its deviatoric part are defined as follows

$$I_1 = \frac{1}{3} \text{tr}[\underline{s}] \quad (3)$$

$$J_2 = \frac{1}{2} \underline{s} : \underline{s} \quad (4)$$

$$J_3 = \det(\underline{s}) = \frac{1}{3} (\underline{s} \cdot \underline{s}) : \underline{s} \quad (5)$$

The von Mises equivalent stress is also defined with respect to  $J_2$

$$\bar{\sigma}_{eq} = \sqrt{3J_2} \quad (6)$$

A stress state can be presented in the space of three principal stresses by a point of  $P(\sigma_1, \sigma_2, \sigma_3)$  as shown in Figure 2. In the same figure, it can also be expressed in the Haigh-Westergaard space by  $(\xi, \rho, \theta)$ .  $\xi$  corresponds to the distance of the origin and the deviatoric plane that stress state  $P$  is located.  $\rho$  is the projection of the vector  $OP$  in the deviatoric plane and  $\theta$  represents the angle between the projection of  $OP$  and the  $\sigma_1$  axis in the deviatoric plane which is the so-called Lode angle. All the components are expressed by the three invariants as follows

$$\xi = \sqrt{3}I_1 \quad (7)$$

$$\rho = \sqrt{2J_2} \quad (8)$$

$$\cos 3\theta = \frac{3\sqrt{3}}{2} \frac{J_3}{J_2^{3/2}} \quad (9)$$

where the Lode angle  $\theta$  is in the range of  $0 \leq \theta \leq \pi/3$ . Consequently, two dimensionless parameters, stress triaxiality and Lode angle parameter, are defined

$$\eta = \frac{\sigma_m}{\bar{\sigma}_{eq}} = \frac{I_1}{\sqrt{3}J_2} \quad (10)$$

$$\bar{\theta} = 1 - \frac{2}{\pi} \cos^{-1} \left( \frac{3\sqrt{3}}{2} \frac{J_3}{J_2^{3/2}} \right) \quad (11)$$

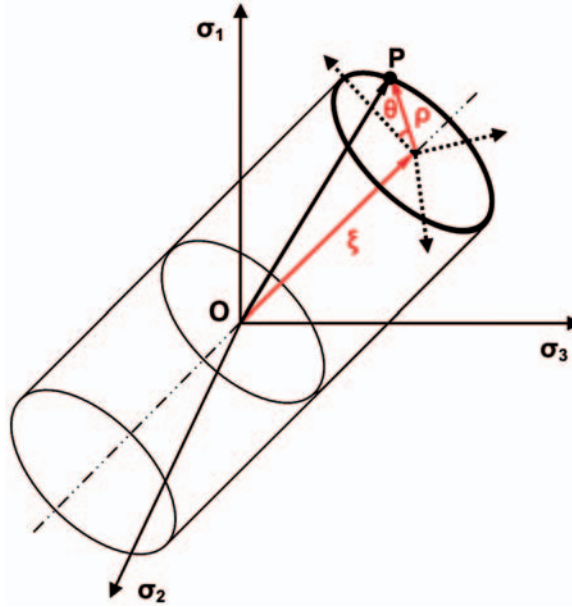


**Figure 2.** Geometric representation of a stress state in the space of principal stresses and Haigh–Westergaard space.

where stress triaxiality,  $\eta$ , is defined by the ratio of the mean stress over the von Mises equivalent stress, while the Lode angle parameter  $\bar{\theta}$  is the normalised Lode angle, which has a range of  $-1 \leq \theta \leq 1$ . Therefore, any stress state can be represented by the combination of these two dimensionless parameters.

### Modelling of plasticity

Under the assumption of isotropic materials and the plastic incompressibility, the yield potential of Bai–Wierzbicki plasticity model for pressure-independent materials in conjunction with an isotropic power-hardening law is defined as follows

$$\Phi(J_2, J_3) = \bar{\sigma}_{eq} - \bar{\sigma}(\bar{\epsilon}) \left[ c_{\theta}^s + (c_{\theta}^{ax} - c_{\theta}^s) \left( \gamma - \frac{\gamma^{m+1}}{m+1} \right) \right] \leq 0 \quad (12)$$

where  $\bar{\sigma}(\bar{\epsilon})$  is the flow curve;  $\gamma$  and  $c_{\theta}^{ax}$  are defined as follows

$$\gamma = \frac{\sqrt{3}}{2 - \sqrt{3}} \cdot \left[ \sec\left(\theta - \frac{\pi}{6}\right) - 1 \right] = \frac{\sqrt{3}}{2 - \sqrt{3}} \left[ \sec\left(\frac{\bar{\theta}\pi}{6}\right) - 1 \right] \quad (13)$$

$$c_{\theta}^{ax} = \begin{cases} c_{\theta}^t, & \bar{\theta} \geq 0 \\ c_{\theta}^c, & \bar{\theta} < 0 \end{cases} \quad (14)$$



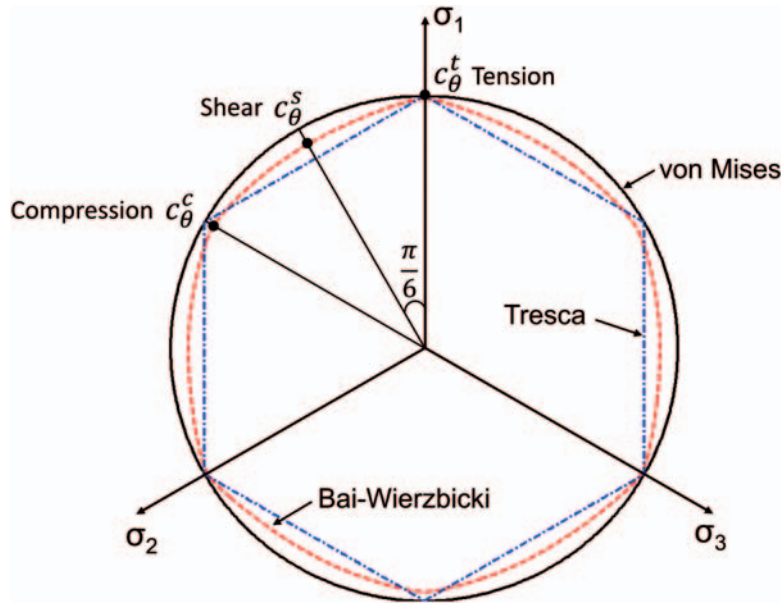


**Figure 3.** Different yield loci on the deviatoric plane, von Mises, Tresca and Bai-Wierzbicki yield criteria ( $c_\theta^t = 1$ ,  $c_\theta^s = 0.93$ ,  $c_\theta^c = 0.97$  and  $m = 5$ ).

where  $c_\theta^t$ ,  $c_\theta^s$ ,  $c_\theta^c$  and  $m$  are material constants. Note that compared to the conventional J2 plasticity in equation (15), the stress–state effect is taken into account by the dependency of the Lode angle parameter which is related to the third invariant of deviatoric tensor.

$$\Phi(J_2) = \bar{\sigma}_{eq} - \bar{\sigma}(\bar{\varepsilon}) \leq 0 \quad (15)$$

As shown in Figure 3, the yield function is formulated by comparing the von Mises and Tresca yield criteria, and  $c_\theta^t$ ,  $c_\theta^s$  and  $c_\theta^c$  are the parameters corresponding to tension, shear and compression stress state, respectively, whereas  $m$  is a non-negative integer in the higher order power term of  $\gamma$  to ensure the smoothness of the yield locus.

Accordingly, the conventional associated flow rule is applied to the present plasticity model.

$$d\varepsilon^p = d\lambda \frac{\partial \Phi}{\partial \sigma} \quad (16)$$

where  $d\lambda \geq 0$  is the scalar plastic multiplier. The detailed derivation of the normal direction with respect to yield locus,  $\frac{\partial \Phi}{\partial \sigma}$ , can be found in Bai and Wierzbicki (2008). Note that without the consideration of the pressure dependency of the yield function, the fully associated flow rule satisfies the assumption of plastic incompressibility.

It can be readily proved that the yield function (equation (12)) satisfies the requirement of differentiability and smoothness. When the associated flow rule is applied, another feature of the yield function, convexity, is a necessary condition to ensure the uniqueness of the solution in numerical simulation (Barlat et al., 2003; Hu and Wang, 2005). For isotropic materials, to prove the convexity

of the adapted yield function without the effect of pressure in this study, only the convexity of the yield locus on the deviatoric plane needs to be proved.

To represent the yield locus in the deviatoric plane, the yield function from equation (12) is transformed to a function in the polar coordinate system by converting  $\bar{\sigma}_{eq}$  into  $\rho$ . Since the yield stress is a positive constant factor, the yield function is simplified to equation (17) in the deviatoric plane.

$$\rho(\theta) = c_{\theta}^s + (c_{\theta}^{ax} - c_{\theta}^s) \left( \gamma - \frac{\gamma^{m+1}}{m+1} \right) \quad (17)$$

The convexity of the function  $\rho = \rho(\theta)$  is preserved if the condition

$$\rho^2 + 2\rho'^2 - \rho\rho'' \geq 0 \quad (18)$$

is satisfied (Jiang and Pietruszczak, 1988), in which  $\rho' = \partial\rho/\partial\theta$  and  $\rho'' = \partial^2\rho/\partial\theta^2$ . With the function of  $\rho = \rho(\theta)$  in equation (17), the inequality required for the sufficient and necessary condition for convexity becomes as follows

$$\begin{aligned} & \left[ c_{\theta}^s + (c_{\theta}^{ax} - c_{\theta}^s) \cdot \left( \gamma - \frac{\gamma^{m+1}}{m+1} \right) \right]^2 + 2 \cdot (c_{\theta}^{ax} - c_{\theta}^s)^2 \cdot \gamma'^2 \cdot (1 - \gamma^m)^2 \\ & - \left[ c_{\theta}^s + (c_{\theta}^{ax} - c_{\theta}^s) \cdot \left( \gamma - \frac{\gamma^{m+1}}{m+1} \right) \right] \cdot (c_{\theta}^{ax} - c_{\theta}^s) \cdot [\gamma'' - m \cdot \gamma^{m-1} \cdot \gamma'^2 - \gamma^m \cdot \gamma''] \geq 0 \end{aligned} \quad (19)$$

where

$$\gamma = \frac{\sqrt{3}}{2 - \sqrt{3}} \left[ \frac{1}{\cos(\theta - \pi/6)} - 1 \right] \quad (20)$$

$$\gamma' = \frac{\sqrt{3}}{2 - \sqrt{3}} \cdot \frac{\sin(\theta - \pi/6)}{\cos^2(\theta - \pi/6)} \quad (21)$$

$$\gamma'' = \frac{\sqrt{3}}{2 - \sqrt{3}} \cdot \frac{1 + \sin^2(\theta - \pi/6)}{\cos^3(\theta - \pi/6)} \quad (22)$$

By evaluating the inequality numerically for various values of parameters,  $c_{\theta}^s$ ,  $c_{\theta}^{ax}$ ,  $c_{\theta}^c$  and  $m$ , the convexity of the yield locus is controlled by  $c_{\theta}^s/c_{\theta}^{ax}$  and  $m$ . The numerically calculated valid range for the convexity of the yield locus is demonstrated in Figure 4. Generally, the range for the convexity is bounded by an upper and lower limit. When  $m = 0$ , the range for  $c_{\theta}^s/c_{\theta}^{ax}$  to satisfy a convex yield locus is  $[0, +\infty]$ . The change of the valid range of  $c_{\theta}^s/c_{\theta}^{ax}$  is extensive when  $m$  is between zero and one. After  $m$  increases from one, the lower and upper limits are approaching to two constant values,  $\sqrt{3}/2$  and 1, respectively. As recommended by Bai and Wierzbicki (2008),  $m$  is selected as a non-negative integer. However, when  $m = 0$ , the effect of the Lode angle is not present in the yield function, as seen from equations (12) or (17). For practical applications,  $m$  as a positive integer is recommended. Therefore, a simple and conservative condition for the convexity of the yield locus is given as independent on  $m$

$$\frac{\sqrt{3}}{2} \leq \frac{c_{\theta}^s}{c_{\theta}^{ax}} \leq 1 \Leftrightarrow \frac{\sqrt{3}}{2} \leq \frac{c_{\theta}^s}{c_{\theta}^c} \leq 1, \quad \text{and} \quad \frac{\sqrt{3}}{2} \leq \frac{c_{\theta}^s}{c_{\theta}^c} \leq 1 \quad (23)$$

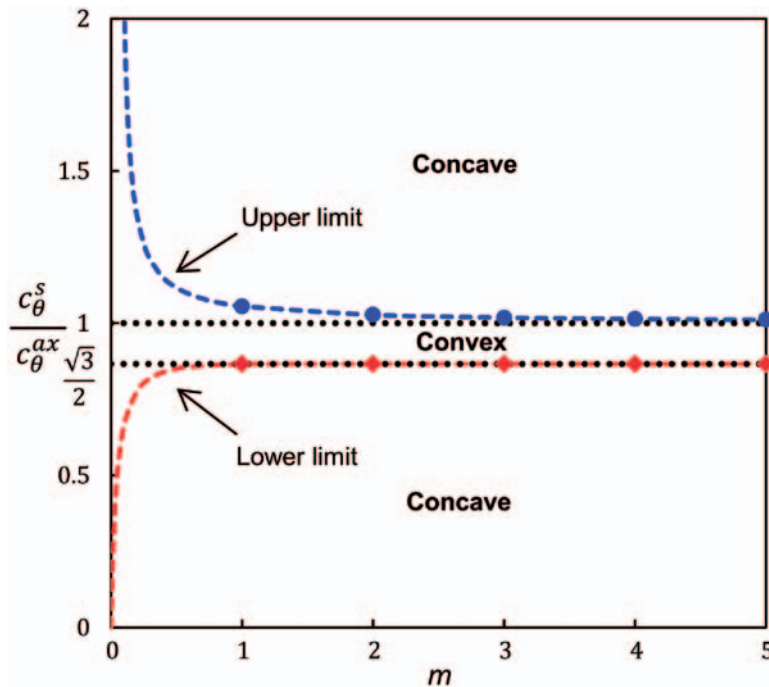


**Figure 4.** Valid range for the convexity of the presented yield locus in the space of  $c_{\theta}^s/c_{\theta}^{ax}$  and  $m$ .

In Figure 5, the yield loci with various values of  $c_{\theta}^s/c_{\theta}^{ax}$ , 0.7, 0.8, 0.887, 0.9, 1.0 and 1.1, are demonstrated at  $m = 5$ . Only the values of the ratio within the valid range (equation (23)) give convex shapes. The reason that  $m$  is not playing a major role in the controlling of the convexity of the yield locus is that it is introduced to satisfy the smoothness of the yield locus only at the Lode angle in the vicinity of 0 or  $\pi/3$ , and the effect of the higher power order term of  $\gamma$  on the main part of the yield locus is negligible. In Figure 6, the yield loci with different values of  $m$ , 0, 1 and 5 are presented at  $c_{\theta}^s/c_{\theta}^{ax} = 0.9$ . The yield locus becomes a circle with the radius of  $c_{\theta}^s$  as von Mises yield criterion at  $m = 0$ . After  $m$  increases from zero, the distances of  $\rho(\theta = 0)$  and  $\rho(\theta = \pi/3)$  are approaching to  $c_{\theta}^s$  and  $c_{\theta}^c$ , respectively; whereas, the shape of the yield locus remains nearly unchanged when Lode angle is around  $\pi/6$ . It is noted that the condition for the convexity can also be interpreted by the geometrical representation. As shown in Figure 3, when  $c_{\theta}^s/c_{\theta}^{ax} = \sqrt{3}/2$ , the yield stress of the present yield locus at  $\theta = \pi/6$  is identical to the one of Tresca criterion. In this case, the Tresca criterion (a straight line from  $\theta = 0$  to  $\theta = \pi/3$ ) represents the limit for a convex shape. Therefore the lower limit of equation (18) is obtained. The upper limit can be similarly observed when considering the convexity of the symmetry of yield locus at three axes. The values of  $\rho(\theta)$  at the axes need to be the maximum to satisfy the convexity of the yield locus, which results in the upper limit of  $c_{\theta}^s/c_{\theta}^{ax} = 1$ .

The plasticity model presented here is taking a general form with the Lode angle correction; by choosing different parameters, it can be reduced into simpler quadratic or non-quadratic yield functions. For example, the von Mises yield function can be obtained by assuming  $c_{\theta}^t = c_{\theta}^s = c_{\theta}^c = 1$  or  $m = 0$ , and the Tresca yield function is given by taking  $c_{\theta}^t = c_{\theta}^c = 1$ ,

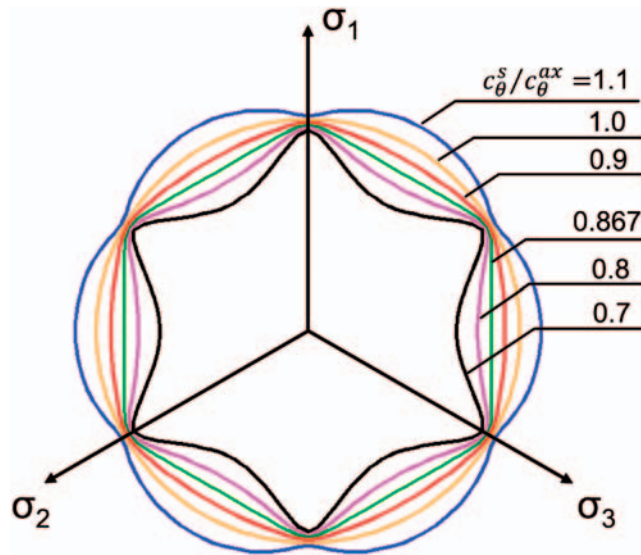


**Figure 5.** The present yield loci with different ratios of  $c_{\theta}^s/c_{\theta}^{ax}$  when  $m = 5$ .

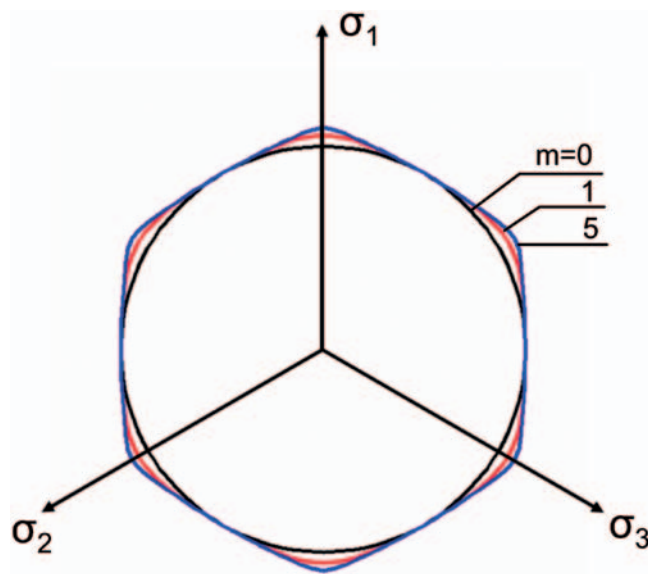


**Figure 6.** The present yield loci with different values of  $m$  when  $c_{\theta}^s/c_{\theta}^{ax} = 0.9$ .

$c_\theta^s = \sqrt{3}/2$  and  $m = +\infty$ . By fixing  $c_\theta^t = c_\theta^c = 1$  and  $m = +\infty$ , the yield function with variation of  $c_\theta^s$  in terms of  $\bar{\sigma}$  and  $\bar{\theta}$  can be one-to-one related to the non-quadratic Hosford yield function with respect to the exponent  $k$ . The reader is referred to Bai and Wierzbicki (2010) for more detailed discussion.

### Modelling of damage onset and evolution

In a commonly used fracture locus, the Rice–Tracey model (Rice and Tracey, 1969) or the simplified Johnson–Cook model (Johnson and Cook, 1985), the fracture strain  $\bar{\epsilon}_f$  takes a form with respect to stress triaxiality  $\eta$ , as shown in equation (24). It is also referred to as the ductile failure curve (Schlüter et al., 1996).

$$\bar{\epsilon}_f = C_1 e^{-C_{2\eta}} \quad (24)$$

The Bai–Wierzbicki fracture locus includes the effect of the Lode angle through a parabolic function of  $\bar{\theta}$ , defined as follows

$$\bar{\epsilon}_f = \left[ \frac{1}{2} (C_1 e^{-C_{2\eta}} + C_5 e^{-C_{6\eta}}) - C_3 e^{-C_{4\eta}} \right] \bar{\theta}^2 + \frac{1}{2} (C_1 e^{-C_{2\eta}} - C_3 e^{-C_{4\eta}}) \bar{\theta} + C_3 e^{-C_{4\eta}} \quad (25)$$

where  $C_1$ – $C_6$  are the material parameters that need to be calibrated from experiments. With these six parameters, the locus generally exhibits an asymmetric feature with respect to the Lode angle parameter. The equation is constructed based on three branches of simple ductile failure curves which correspond to the Lode angle parameter as 1, 0 and  $-1$ , respectively. Each pair of parameters describes an exponential function of one branch of the ductile failure curve; that is,  $C_1$  and  $C_2$ , correspond to  $\bar{\theta} = 1$ ,  $C_3$  and  $C_4$  correspond to  $\bar{\theta} = 0$ , and  $C_5$  and  $C_6$  correspond to  $\bar{\theta} = -1$ . In this study, the same form of the phenomenological equation as equation (25) is used, but to characterise the onset of damage, that is, the crack initiation strain  $\bar{\epsilon}_i$ , rather than the fracture strain  $\bar{\epsilon}_f$ .

After the onset of damage, the isotropic damage evolution is assumed. As an analogy to the CDM-based models, an internal variable  $D$  is introduced to measure the accumulated damage. Following the hypothesis of strain equivalence (Lemaitre, 1992), the strain behaviour of a damaged material is represented by constitutive equations of a virgin material (without damage) in the potential of which stress is simply replaced by effective stress; the damage-plasticity yield function is consequently extended from equation (12) to the following expression

$$\Phi(J_2, J_3, D) = \bar{\sigma}_{eq} - \bar{\sigma}(\bar{\epsilon}) \left[ c_\theta^s + (c_\theta^{ax} - c_\theta^s) \left( \gamma - \frac{\gamma^{m+1}}{m+1} \right) \right] (1 - D) \leq 0 \quad (26)$$

The dissipation-energy-based damage evolution law applied in finite element (FE) code (ABAQUS, 2011) is adopted.

$$\dot{D} = \frac{\sigma_{y0} L}{2G_f} \dot{\bar{\epsilon}} \quad (27)$$

where  $G_f$  is the energy required to open a unit area of a crack,  $L$  is the characteristic length associated with an integration point to reduce the mesh dependency in the FE model and  $\sigma_{y0}$  is

the value of the yield stress at the onset of damage. The final fracture is reached when the damage  $D$  is accumulated to a critical value  $D_{cr}$ .

$$D_{cr} = \int_{\bar{\varepsilon}_i}^{\bar{\varepsilon}_f} \frac{\sigma_{y0} L}{2G_f} d\bar{\varepsilon} \quad (28)$$

Depending on the loading process,  $D$  is consequently distributed in the following range

$$D = \begin{cases} 0; & \bar{\varepsilon} \leq \bar{\varepsilon}_i \\ \int_{\bar{\varepsilon}_i}^{\bar{\varepsilon}} \frac{\sigma_{y0} L}{2G_f} d\bar{\varepsilon}; & \bar{\varepsilon}_i < \bar{\varepsilon} < \bar{\varepsilon}_f \\ D_{cr} & \bar{\varepsilon} = \bar{\varepsilon}_f \end{cases} \quad (29)$$

The formulated model was numerically implemented into FE code ABAQUS/Explicit as a VUMAT subroutine for the modelling of the material plasticity and damage behaviour.

### Methodology of material parameters calibration

Based on the description of the three main constituents of the damage modelling approach, there are parameters at different deformation stages that need to be calibrated. A hybrid experimental and numerical approach is employed to conduct the calibration as follows:

- Carry out a series of tests that covers a broad range of stress states.
- Record the force–displacement response during the whole deformation until fracture, and determine the crack initiation instant and location.
- Perform the corresponding simulations only with the chosen plasticity model.
- Calibrate the parameters of the plasticity model based on the comparison of global force–displacement responses between experiments and simulations until the onset of damage.
- Access the local variables, equivalent plastic strain, stress triaxiality and Lode angle parameters, from the simulation with calibrated parameters of the plasticity model at the experimentally determined crack initiation instant and location.
- Calibrate the parameters for the ductile crack initiation locus.
- Perform simulations for selected specimens with the crack initiation threshold and damage-induced softening.
- Calibrate the parameters for damage-induced softening based on the comparison of global force–displacement responses between experiments and simulations until the final fracture.

The methodology to determine both the microscopic crack initiation instant and location from experiments is discussed below.

### Identification of damage instant

In the literature, observation by eye or digital image correlation is normally conducted to detect the macrocrack formation (Bao and Wierzbicki, 2004a; Dunand and Mohr, 2010). It gives a characteristic length of crack with an order of 0.1 mm. In this study, the direct current potential drop (DCPD) method is developed to detect the microcrack initiation. This method has been used to determine the

onset of stable crack initiation in fracture mechanics tests. It is transferred to the study of damage mechanics due to its simplicity and ability to detect microscopic material degradation.

A schematic setup of experiments is demonstrated in Figure 7. At the points ( $I$ ,  $I'$ ), a constant direct current is conducted to the specimen. The amperage is selected according to the material and the dimension of the specimen to avoid critical heating on the specimen. Plastic insulators are mounted on two sides of the specimen-clamping systems to prevent current leakage. Two metal pins are welded onto two sides of the gauge section ( $V$ ,  $V'$ ) and connected to a voltmeter to record the potential drop during the test. The initial application of the method and the correlation of it to microscopic mechanisms were introduced by Münstermann (2006). As shown in Figure 8(a), the potential slightly increases at the beginning of the test due to the progressive reduction of the area of the cross section caused by the incremental loading. At a particular phase of the experiment, due to the appearance of severe discontinuity induced by the coalescence of voids or the formation of microcrack or shear bands, the electrical resistance/potential increases suddenly. This time instant is assumed as the crack initiation and the corresponding force as the critical load. To verify the correct detection of the crack initiation and correlate the response of current potential to the underlying damage mechanisms, a program involving interrupted tests in conjunction with subsequent metallographic investigations was performed. Identical notched specimens were loaded to different forces in the vicinity of the critical force obtained from the DCPD method. The specimens were subsequently prepared for the metallographic investigation from the interrupted tests. The voids coalescence was not successfully observed from the light optical microscopy (LOM) until the specimen was loaded to the critical force. The micrograph at the crack initiation point is shown in Figure 8(b). As seen from the LOM graph, this method provides a detection of damage with the length scale of dozens of microns. The main advantage of the method is its easy installation and proceeding to couple with the laboratorial experiment facility, though the quantitative correlation between the microscopic material behaviour and the macroscopic parameter that determines the damage still needs to be explicitly defined.

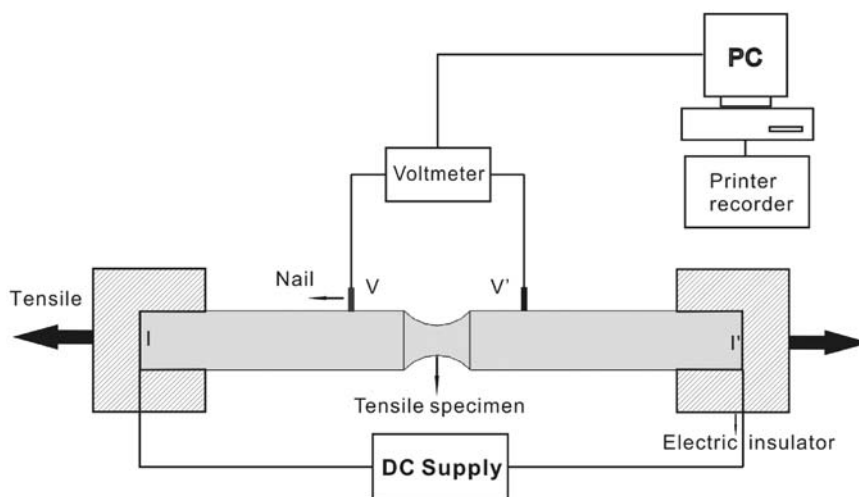


**Figure 7.** Direct current potential drop method for the determination of crack initiation during tensile test.



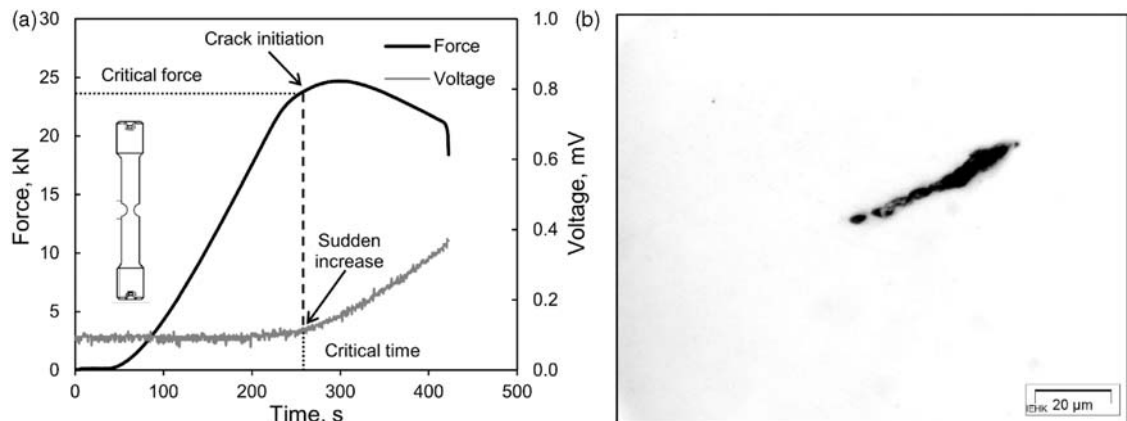


**Figure 8.** (a) A plot of force and electric potential versus time curves. (b) Micrograph of the occurrence of void coalescence at the crack initiation point.

### Identification of damage location

In the literature, it has been widely accepted that the location of the onset of fracture coincides with the location of the highest equivalent plastic strain within the specimen at the instant of fracture. Due to the limits in detecting the instant of fracture, this location is often on the surface of specimens. This assumption works well when the analysis is focused on a macroscopic failure such as the final fracture. However, when a microscopic crack initiation instant is adopted, a more sophisticated procedure needs to be carried out. In this study, firstly, a microscopic digital camera is attached to monitor the specimen surface at the gauge section during the history of testing. The crack initiation location that occurs on the surface of the specimen is therefore captured by the camera. Secondly, a post-fracture metallography study is carried out. To detect the accurate crack initiation location, the fracture mode and the underlying damage mechanisms that control the whole process are investigated. Scanning electron microscopy (SEM) fractography is therefore employed to identify the dominating damage mechanism, dimple or shearing. In addition, the correlation of damage mechanisms and the stress state is also discussed.

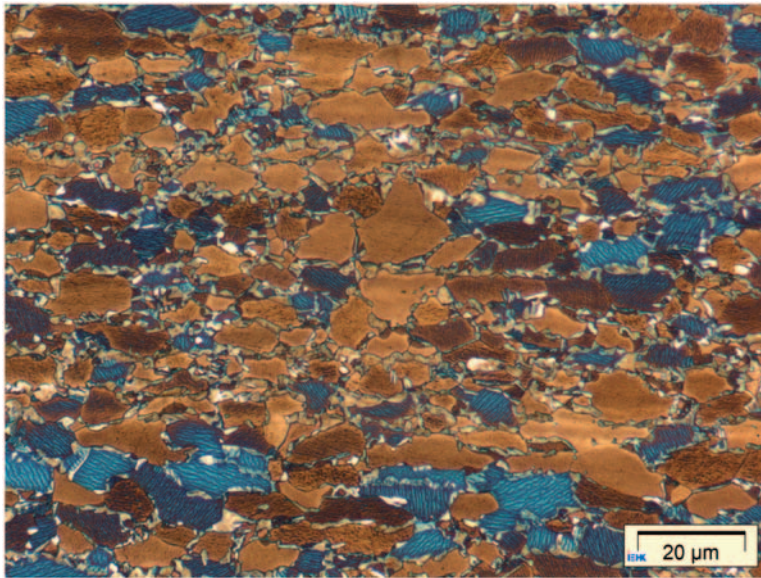
### Materials

Dual-phase steel is a classic representative of AHSS. DP600 is therefore chosen as the material for the present study. The chemical composition of DP600 steel is shown in Table 1 and the microstructure is shown in Figure 9. It consists of ferrite, martensite and minor retained-austenite. More than 10% martensite is responsible for the elevated strength compared to single-phase ferritic steel. The actual phase volume fraction determined using four specimens is shown in Table 2 and also compared with the typical values for DP steel. The tested standard mechanical properties are listed in Table 3.



**Table 1.** Chemical composition of the DP600 steel, mass contents in percentage.

C	Si	Mn	P	S	Mo	N
0.11	0.39	1.38	0.017	<0.001	0.0515	0.004

**Figure 9.** Light optical microscopic photo of DP600 microstructure.

## Material parameters calibration

### *Calibration of the stress-state effect on plastic behaviour*

According to parameter description in Bai and Wierzbicki (2008),  $c_{\theta}^t$  is equal to 1, since the stress–strain description is obtained from a smooth dog-bone tensile test. Only  $c_{\theta}^s$ ,  $c_{\theta}^c$  and  $m$  remain unknown. In this study, both dog-bone and plane-strain specimens with varied geometries under tension are used to calibrate  $c_{\theta}^s$  and  $m$ . Because the stress states at different deformed locations are not the same, more stress states are considered than in the conventional calibration strategy (Bai and Wierzbicki, 2008) to achieve better fitting results. Due to the difficulty in performing upsetting tests for sheet materials, a hydraulic bulge test is conducted to calibrate  $c_{\theta}^c$ .

Dog-bone and plane-strain tensile tests. All the specimens used in this study are extracted from a DP600 steel sheet with a thickness of 1.5 mm. They are cut such that the loading direction of the specimen was orientated along the rolling direction. All the uniaxial tension tests are performed on a hydraulic tensile testing machine ‘Zwick 1484’. To achieve a quasi-static condition, a low crosshead speed is applied at 0.3 mm/min. The special customised clamping system to measure the electric potential during the test is employed for all the tests.

**Table 2.** Typical and actual phase volume fraction for DP600 steels.

Phase		Ferrite 70–90	Martensite 10–30
Average volume fraction for DP steels (%)			
Measured phase volume fraction for DP600 steels (%)	Transverse dir. sample 1	77	18
	Transverse dir. sample 2	79	17
	Longitudinal dir. sample 1	79	18
	Longitudinal dir. sample 2	77	18

**Table 3.** Mechanical properties of DP600 steels.

Young's modulus, $E$	Yield strength, $R_{p0.2}$	Ultimate tensile strength, $R_m$	Uniform elongation, $A_g$	Fracture elongation, $A_5$
214 GPa	390 MPa	704 MPa	16.5%	23%

Three different geometry configurations of dog-bone specimens are designed as shown in Figure 10. Notches with circular cuts, ‘U’ and ‘V’ shapes are used to generate various stress states. The first configuration produces the closest stress state to uniaxial tension. The decreased notches provide a stress state between uniaxial tension and plane-strain condition.

The FE code ABAQUS/Explicit is employed to carry out the numerical analysis. All the specimens are modelled in three dimensions. Considering the symmetry of the specimen geometry and load condition, only 1/8 of the specimen is modelled. Three-dimensional (3D) eight-node solid elements with reduced integration (C3D8R) are used for all cases. The mesh is designed in a way that, in the plastically deformed area, the element size is small and gradually increases towards the only elastically deformed area. Before the calibration of parameters, the mesh dependency is studied. Three different mesh sizes, 0.2 mm, 0.1 mm and 50  $\mu\text{m}$ , are employed. Based on the comparisons of force and equivalent plastic strain versus displacement responses, the influence of the mesh size is negligible. Therefore the medium mesh size, 0.1 mm, is chosen for all the FE models in the study. Moreover, this mesh size is also of importance under the consideration for the element removal described in the section *Calibration of the damage evolution function*. The configuration of mesh conducted for dog-bone specimens is also applied for the rest of the specimens.

The design of plane-strain specimens is illustrated in Figure 11. The width of all the specimens is 50 mm and the height is 130 mm. In all five different radii of the grooves, 15 mm, 12.5 mm, 7.5 mm, 4 mm and 1.5 mm, are manufactured. For the FE modelling, 1/8 of the specimen is used due to the symmetry.

All the dog-bone and plane-strain FE models are run with the user material subroutine (VUMAT). Only the plasticity model is active and the functions of crack initiation and the damage evolution is switched off in the calculation. To calibrate  $c_\theta^s$  and  $m$ , an iterative program is defined as follows:

- perform the simulations of corresponding tests with initially guessed parameters,
- compare the force–displacement curve obtained from the simulation to the experimental record prior to the crack initiation,

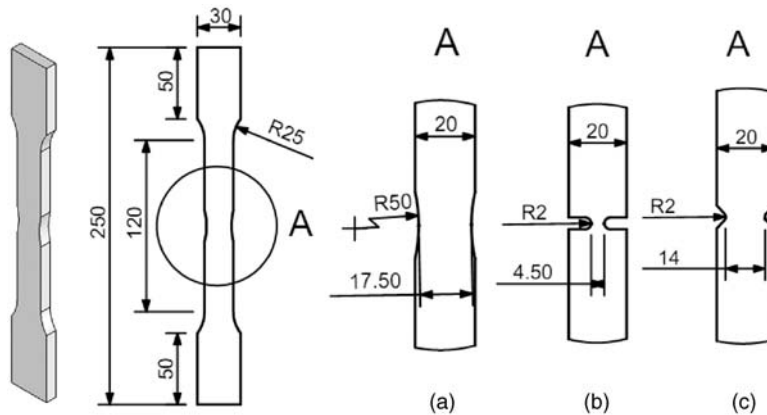


**Figure 10.** Geometry of dog-bone specimens with (a) circular cut-out, (b) 'U' notch and (c) 'V' notch.

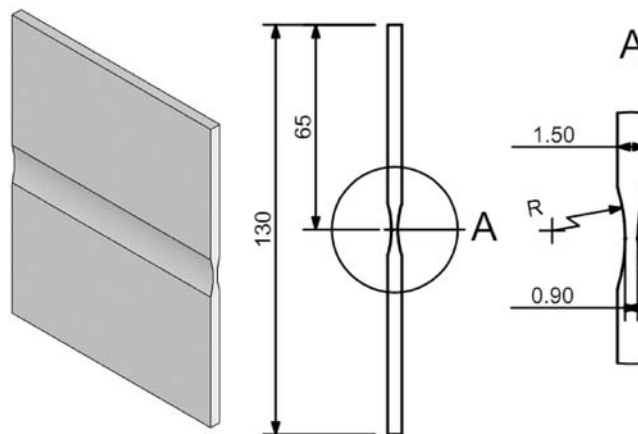


**Figure 11.** Geometry of plane-strain specimens with transverse notches of different radii.

- c. modify the value of parameters based on the deviation exhibited from the comparison and
- d. repeat steps (a)–(c) till the difference between experimental and numerical force–displacement curves for all the tests is minimised.

The calibrated  $c_0^s$  and  $m$  are 0.93 and 5.0, respectively. The comparison of the force–displacement curves between experiments and simulations with different yield criteria for dog-bone and plane-strain tensile tests is shown in Figure 12. For both specimens, von Mises criterion overestimated the force with an error of about 2.3% and 2.2%, respectively, while with the Lode correction the relative errors of the force prediction for both cases are reduced to less than 1%. Note that the error is only calculated until the point of crack initiation, and the subsequent mechanical behaviour will be subjected to the damage-induced softening correction. Here, only the comparison of the dog-bone

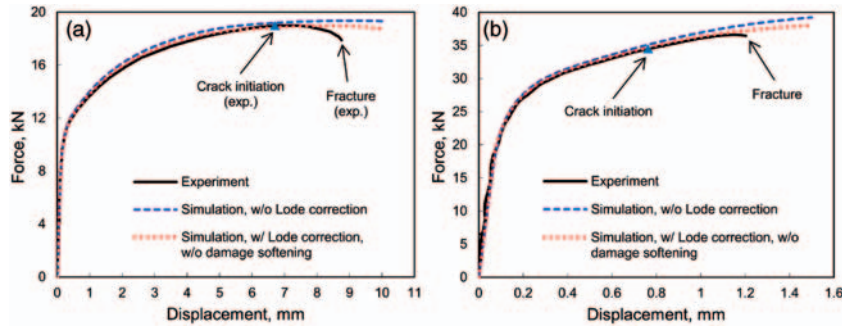


**Figure 12.** Comparison of the experimental and numerical load versus displacement curves for (a) the dog-bone specimen ( $R = 50$  mm) and (b) the plane-strain specimen ( $R = 7.5$  mm).

specimen ( $R = 50$  mm) and the plane-strain specimen ( $R = 7.5$  mm) is demonstrated for the respective group. The other geometries behave likewise.

**Bulge test.** The bulge test is characterised by a biaxial stress and strain state. In the test, a circular blank with a diameter of 160 mm is clamped along its perimeter. The hydraulic pressure is applied to the lower surface of the blank through the oil under the compression of the displacement-controlled punch. The velocity of the punch is pre-assigned at 15 mm/min. During the loading, a bulge occurs and costs thinning of the material, as schematically shown in Figure 13. A measuring method with a laser light section for geometry analysis and a camera device for local strain determination are attached (Uthaisangsuk, 2009).

In the FE simulation, a quarter of the whole test assembly is modelled because of the geometrical symmetry. In the model, the drawing die and blank holder are modelled as rigid bodies. A surface-to-surface contact is applied between the specimen and the drawing die, as well as between the specimen and the blank holder with a friction coefficient of 0.3. The same iterative procedure is performed with the previously calibrated  $c_\theta^s$  and  $m$  to determine  $c_\theta^c$ . As shown in Figure 14, the pressure predicted by von Mises plasticity is beyond the experimental data. With a fitted value of  $c_\theta^c$  as 0.97, a good agreement with the experimental curve is achieved.

### Calibration of the ductile crack initiation locus

In this section, three different types of tensile test are adopted to calibrate the corresponding parameters, central-hole, pure-shear and plane-strain tests. To obtain the data points in the space of  $\eta$ ,  $\bar{\theta}$  and  $\bar{\varepsilon}_i$ , the crack initiation instant and location need to be determined from experiments by the DCPD method and fractography analysis. Note that only the fractured surfaces of the specimens are subjected to the investigation. The local data history of these variables at the critical spot is obtained from the subsequent numerical simulations.

**Central-hole tensile test.** Two types of geometry configurations are designed, differing in the cutting shape at the centre of specimens (Figure 15). The first type is a circular cut with a radius of 3 mm. The other configurations feature an elliptical cut at the centre with a constant minor radius of 2 mm and varied major radii of 3, 5 and 7 mm. The fractured surface of the central-hole specimen is shown in Figure 16. A 'V'-shape fracture mode is observed at the inner edge of the hole and extended along the transverse axis. The crack is initiated at the intersection of the circular cut and the transverse axis in the middle plane of the specimen. The SEM fractographs are investigated at

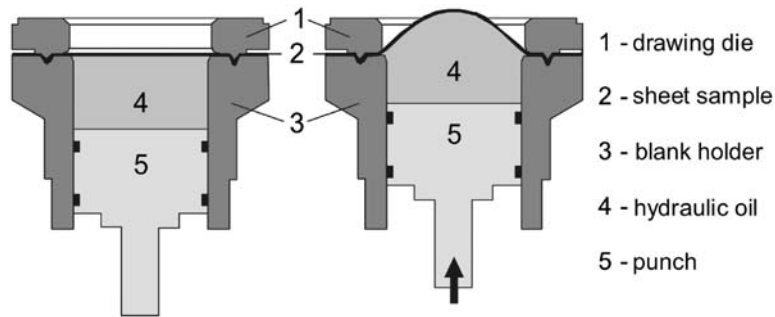


**Figure 13.** Schematic representation of the setup of a hydraulic bulge test.

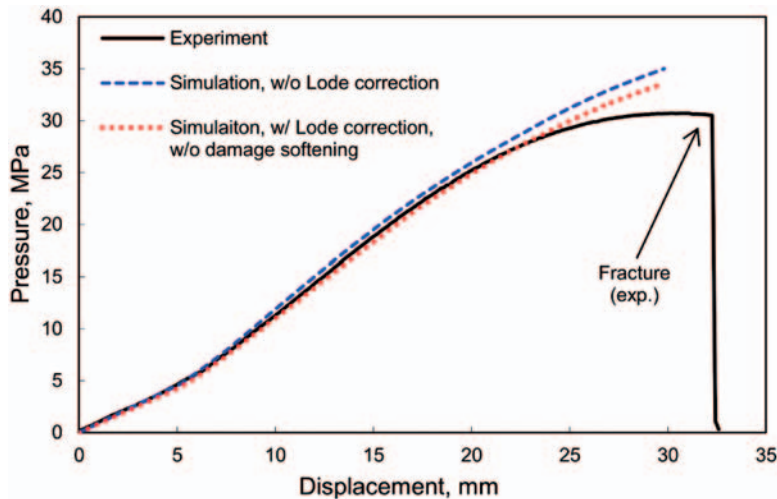


**Figure 14.** Comparison of the experimental and numerical load versus displacement curves for the bulge test.

the crack initiation spot to analyse the corresponding damage mechanisms. As shown in Figure 16, a mass of voids can be observed. They are mostly presented in spherical shapes, except for some linked or enlarged voids. Most voids are relatively large and at the similar size. This type of void is often referred to as the primary void, while the other type of void with smaller size is referred to as the secondary void, which is assumed to be nucleated during the primary voids coalescence at smaller microstructural constituents (Münstermann et al., 2007). A limited number of secondary voids is observed.

After the numerical simulation, as it can be seen in Figure 17, the strain is concentrated at the region where the crack initiation was observed in the experiment. The corresponding local data for all geometry configurations are extracted at the same spot and plotted in Figure 17. For each configuration, the stress triaxiality and Lode angle parameter are almost constant during the deformation history. This behaviour facilitates the minimisation of the error which resulted from

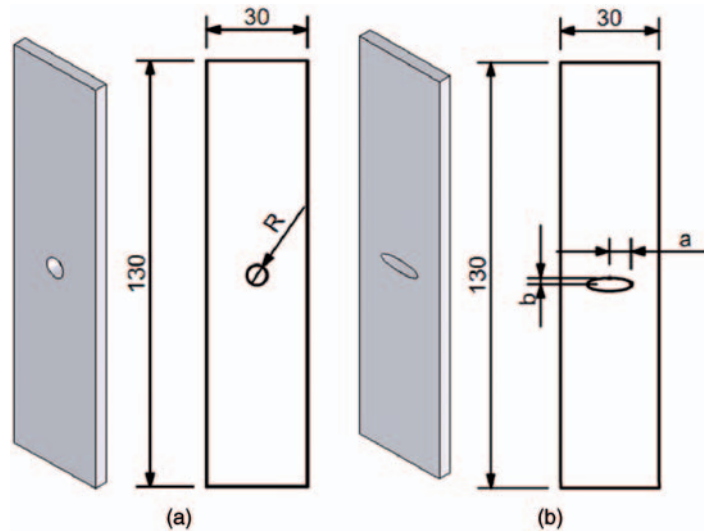


**Figure 15.** Geometry of central-hole specimens with (a) a circular cut-out and (b) an elliptical cut-out.

the experimental crack initiation determination in the comparison of the dog-bone specimens, of which the stress triaxiality and Lode angle parameters both exhibit an increasing trend as the load increases. Bao (2004) studied the influence of the circular cut radius on the stress triaxiality and showed that there was no obvious change of the stress state (uniaxial) with only varied circular cut radii. However, in the present study, by change of the  $a/b$  ratio of the elliptical cut, more stress states in addition to uniaxial tension are generated with increased stress triaxiality and decrease of Lode angle parameter, as shown in Figure 17.

**Pure-shear tensile test.** A pure-shear specimen is designed to achieve lower stress triaxiality in the region of zero Lode angle parameter at a uniaxial tensile test machine. The design is adopted from the work of Bao and Wierzbicki (2004b) and Brunig et al. (2008). Figure 18 shows the design of the pure-shear specimen. An out-plane notch between the two holes in the middle of the specimen is manufactured on both sides to achieve an explicit damage initiation spot. As shown in Figure 19, a flat shearing fracture mode is observed. It can be determined that the crack initiation spot is on the edge of the thinnest part of the specimen close to the holes. In contrast to the void-dominant mechanism, the cause of damage in the pure-shear specimens is the formation of shear bands.

Due to the symmetry in the thickness direction,  $1/2$  of the specimen is modelled. In Figure 20, one can see that the strain is concentrated at the same place as observed in fractographs. The local variables, stress triaxiality, Lode angle parameter and equivalent plastic strain, are extracted at that element and plotted. The Lode angle parameter keeps constant at 0 during the whole deformation, and the stress triaxiality deviates from 0 with a small number between 0.05 and 0.08. It is proved that with the current design of the specimen, shear stress state is achieved by the uniaxial tension loading.

**Plane-strain tensile test.** The global force and displacement history and the critical load to crack initiation for plane-strain specimens were obtained in the section *Dog-bone and plane-strain tensile tests*. Only the critical location, at which the local variables are extracted, needs to be identified. The studies on fracture surface morphology and subsequent SEM fractographs are performed. As shown in Figure 21, the fracture mode is a mixture of 'V'-shape fracture and slant fracture. At the centre of



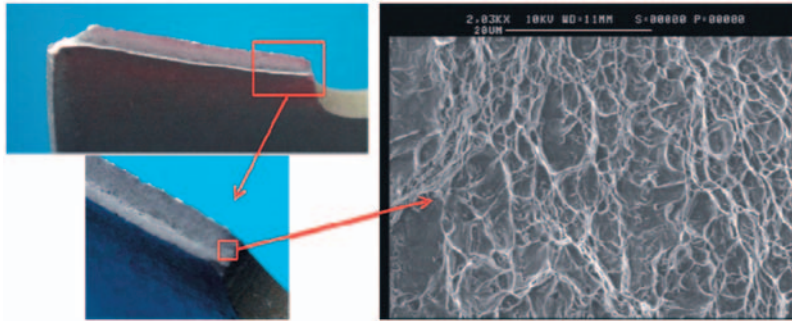


**Figure 16.** Fractographs of central-hole specimen.

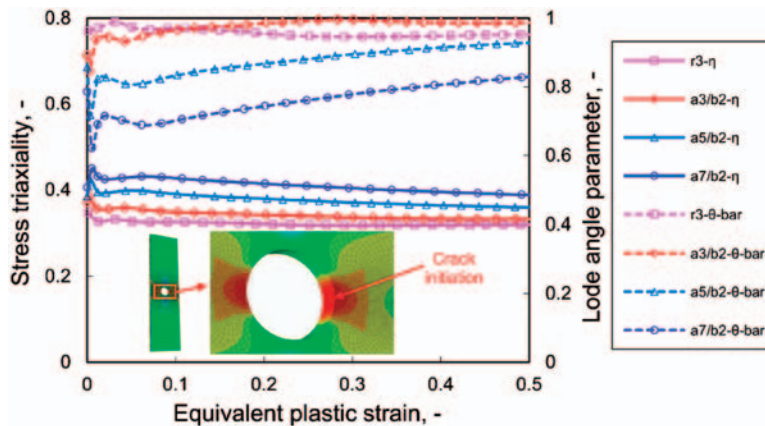


**Figure 17.** History of stress triaxiality and Lode angle parameter for central-hole specimens.

the specimen, the ‘V’-shape fracture mode is present. It extends along the transverse axis in both directions. At a certain point, the fracture mode becomes unstable and transmits into a slant fracture. At the end of the specimen, in the transverse direction, a diffused neck is also formed. On the other hand, the crack initiation is not found at the surface of the specimen from the camera attached on the tensile machine. It can be determined that the crack initiation takes place at the centre of the specimen and propagates through the transverse and thickness directions. As observed in the subsequent SEM fractographs, the void-controlled damage mechanism is dominant. In contrast to the central-hole specimen, the secondary voids in this case account for the major fraction.

As shown in Figure 22, the stress triaxiality of specimen  $R = 15$  mm starts with 0.57 (the initial stress triaxiality of the plane-strain tension stress state) and increases gradually with the deformation. The Lode angle parameter starts, by contrast, with a slight deviation from 0 but reaches 0 with further loading. With the decreased radius of the notch, the stress triaxiality increases accordingly, but the Lode angle parameter continues to follow the similar trend. This guarantees that various stress states are achieved at the crack initiation at the region of the low Lode angle parameter.

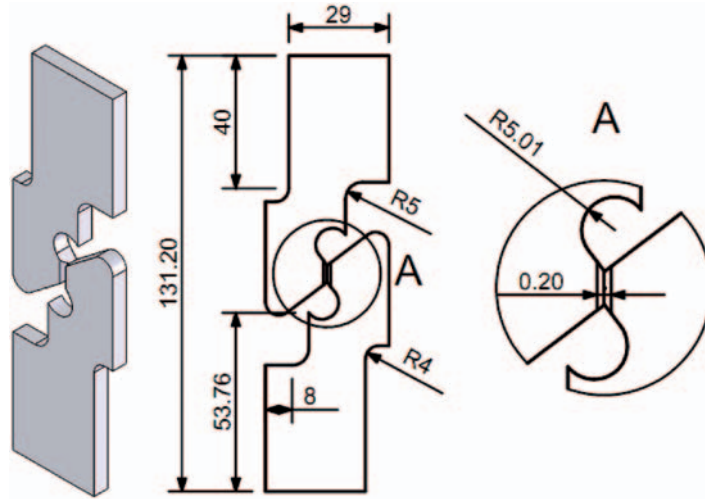


**Figure 18.** Geometry of pure-shear specimen.

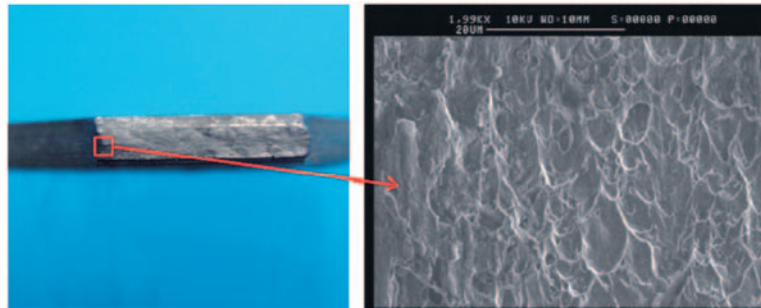


**Figure 19.** Fractographs of pure-shear specimen.

Ductile crack initiation locus fitting. With the histories of  $\eta$ ,  $\bar{\theta}$  and  $\bar{\epsilon}_i$  obtained from the simulation and the critical instant of crack initiation from experiments, the experimental data points are determined. These data points are subsequently used to calibrate the ductile crack initiation locus. One should note that neither compression nor the biaxial tension test is introduced due the technical difficulties in conducting the tests or the crack initiation measurement system. No data in the negative Lode angle region is therefore accessible from the experiments. A symmetric crack initiation locus with only  $C_1$ – $C_4$  defined in equation 30 is employed.

$$\bar{\epsilon}_i = [C_1 e^{-C_2 \eta} - C_3 e^{-C_4 \eta}] \bar{\theta}^2 + C_3 e^{-C_4 \eta} \quad (30)$$

The conventional calibration procedure employed by Bai and Wierzbicki (2008), in which  $C_1$  and  $C_2$  are fitted by the central-hole specimen and  $C_3$  and  $C_4$  are fitted by the plane-strain specimens and pure-shear specimen, is not used here. Based on the quantitative study of the history of the local



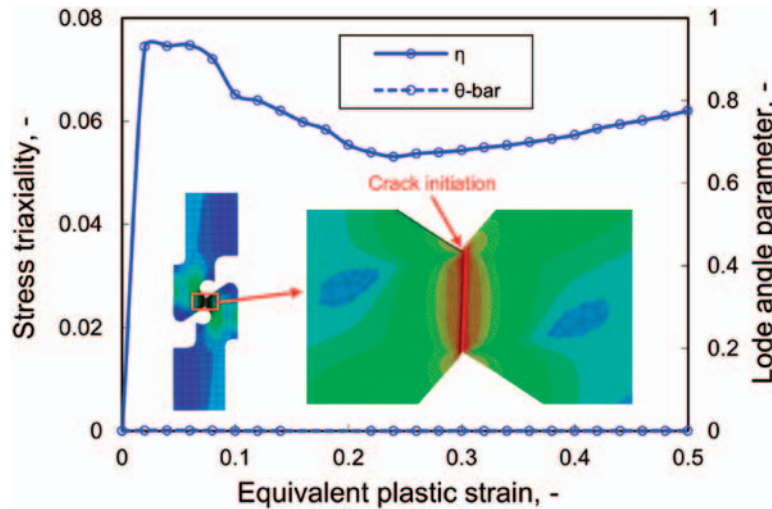


**Figure 20.** History of stress triaxiality and Lode angle parameter for pure-shear specimen.

variables, the values of  $\eta$  and  $\bar{\theta}$  are not constant in the entire deformation process, and more importantly,  $\bar{\theta}$  also deviates from 1 and 0 for central-hole and plane-strain specimens, respectively, when the geometry is varied, as demonstrated in Figures 17 and 22.

Consequently, four parameters are calibrated based on all the data points obtained from the three types of experiments using the nonlinear least square surface fitting in Matlab. The calibrated symmetric ductile crack initiation locus and the experimental data used to calibrate the parameters are shown in Figure 23. The corresponding equation with the calibrated parameters is as follows

$$\bar{\varepsilon}_i = [0.43e^{-1.14\eta} - 0.12e^{-0.98\eta}]\bar{\theta}^2 + 0.12e^{-0.98\eta} \quad (31)$$

### Calibration of the damage evolution function

With the previously calibrated parameters, the material behaviour is characterised till the moment of crack initiation. Once this stage is reached, the damage-induced softening plays a significant role during the post-crack-initiation deformation. In this section, the parameters,  $G_f$  and  $D_{cr}$ , need to be determined from the experiments.

By comparing the experimental and numerical material responses, an iterative procedure is employed to identify  $G_f$ . Depending on the data chosen for the comparison, there are two approaches to carry out the iterative procedure:

- An approach based on the true stress–strain curve.
- An approach based on the force–displacement of certain geometry configuration of tests.

One should note that both of these two sets of data need to contain the material response information from the beginning of the deformation to the final fracture. Considering the numerical cost

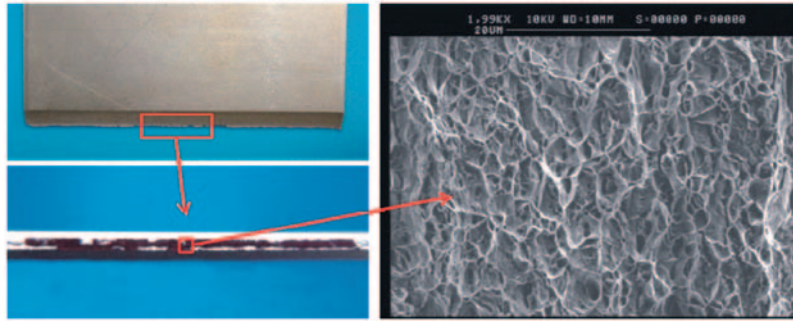


**Figure 21.** Fractographs of plane-strain specimen.

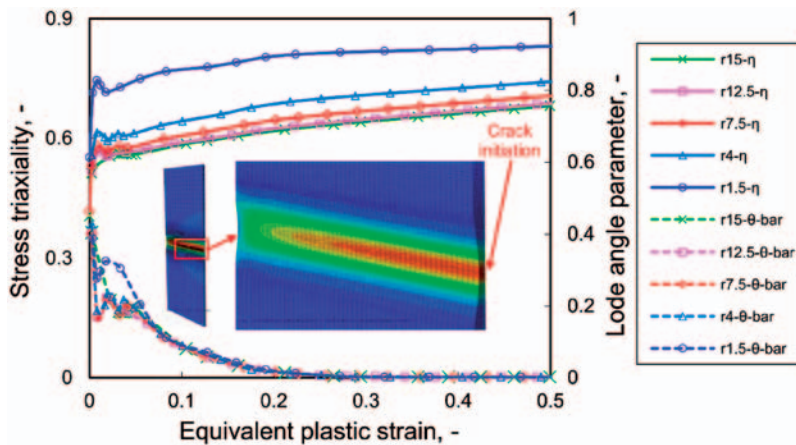


**Figure 22.** History of stress triaxiality and Lode angle parameter for plane-strain specimens.

and time effort, this first approach is easier to achieve. To obtain the numerical stress–strain curve, only a unit cell element tensile or compression test needs to be conducted. On the other hand, the experimental true stress–strain curve till the final fracture is difficult to obtain. Mirone (2004) proposed a phenomenological formula for true stress and strain curve after necking for a round bar tensile test. However, the procedure to validate the formula is rather complex, and its application to the sheet tensile test has not been verified. Therefore, in this study, the second approach is adopted. The experimental data for this approach, in contrast to Mirone's, is easy to access, while the numerical cost is rather high.

The dog-bone specimen with circular cut ( $R = 50$  mm) is chosen to be the reference experimental result. The corresponding numerical simulation results with different  $G_f$  values are compared with the experimental one, as shown in Figure 24(a). It can be determined that the force–displacement curve with  $G_f$  of 300 fits the experimental result best before the occurrence of the final fracture. To predict the macrofracture,  $D_{cr}$  is, therefore, calibrated based on the same specimen. As shown in Figure 24(b), a good agreement is achieved when  $D_{cr}$  is considered as 0.1. Once  $D_{cr}$  is reached for all

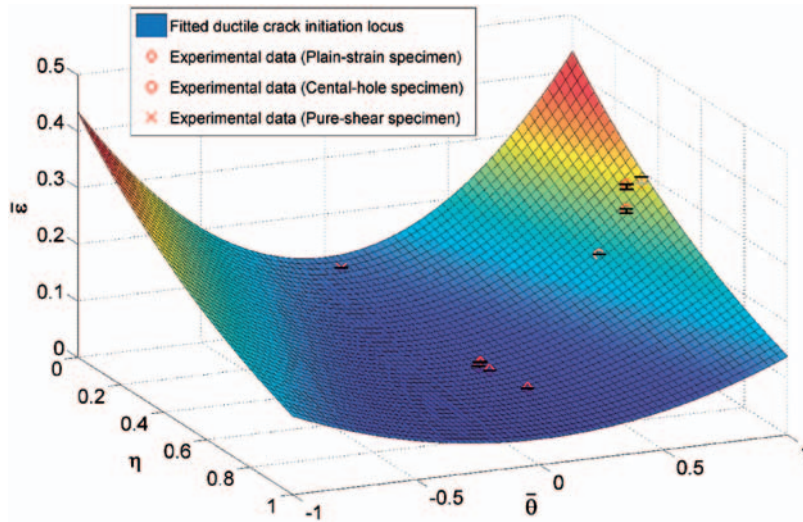


**Figure 23.** Ductile crack initiation locus and experimental data points of DP600 in the space of stress triaxiality  $\eta$ , Lode angle parameter  $\bar{\theta}$  and equivalent plastic strain  $\bar{\epsilon}$ .

the integration points in an element, it is considered that the load-carrying capability of this element is totally lost, and the element is removed from the model for the following computation by the element deletion technique. The mesh size is therefore sensitive to the solution. In this study, a mesh size of  $0.1 \times 0.1 \times 0.1$  mm is employed. It is small enough that the mesh dependency of local variables is not pronounced. More importantly, it also corresponds to the characteristic size of the macrocrack formation observed by eye. On the other hand, the characteristic length  $L$  associated with an integration point is introduced to the formulation of  $D$ . The mesh dependency in the finite element model is therefore reduced during the damage softening part by this intrinsic length. However, the calibrated parameters are consequently related to the mesh size. Thus, a consistent mesh size is conducted in the calibration models, as well as the following verification simulations.

## Validation and discussion of the damage model and calibrated parameters

### Failure prediction of plane-strain tensile test

A plane-strain tensile test was used in the calibration of both plasticity and crack initiation locus parameters, except for the determination of  $G_f$  and  $D_{cr}$ . The complete set of parameters is first applied to this specimen to predict the materials behaviour from the plastic deformation to the final fracture. The experimental and numerical force–displacement responses are compared in Figure 25. During the first phase, a good agreement is achieved till the crack initiation. Secondly, the crack initiation point is compared to validate the parameters for the crack initiation locus. In the simulation, this point is obtained at the moment when the first element in the model reaches the damage threshold. Compared with the experimental result, almost the same displacement to the crack initiation is predicted by the numerical simulation. However, the displacement to the final failure is estimated by the simulation at about 10% more than the experimental result. The reason for the over-prediction lies in the description of the damage evolution. The current model assumes that the

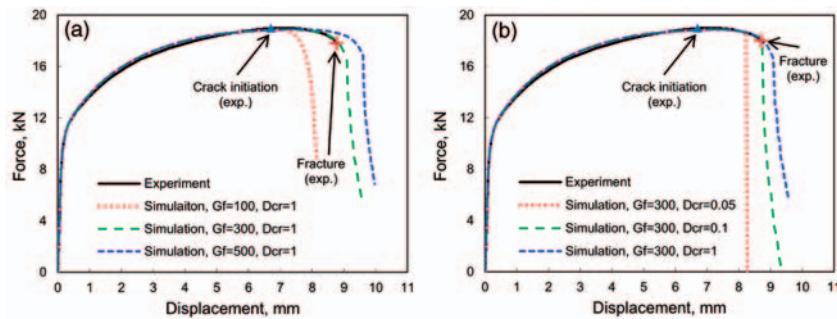


**Figure 24.** Comparison of the experimental and numerical load versus displacement curves for the dog-bone specimen ( $R = 50$  mm) (a) to determine the value of material parameter  $G_f$  and (b) to determine the value of material parameter  $D_{cr}$ .

onset of damage is dependent on the stress state, whereas the internal damage variable  $D$  relies only on the accumulated plastic strain, not yet depending on the stress state, that is, the stress triaxiality and Lode angle parameter. Nevertheless, due to the implementation of the crack initiation threshold which depends on the stress states, the prediction is improved from the modelling based on the conventional CDM model (Teng, 2008).

### Failure prediction of bulge test

The bulge test was used only to calibrate the parameters in the plasticity model. With the further-calibrated parameters from other tests, the numerical prediction of the pressure–displacement response is compared to the experimental one in Figure 26. Due to the difficulty in attaching the measurement instruments, the comparison between experimental and numerical results on the crack initiation points is not conducted. Before the crack initiation point detected by simulation, the von Mises plasticity model gives a relative error about 5%, while with the Lode correction the error reduces to less than 2%. In the whole process of the deformation, the numerically predicted pressure–displacement response coincides with the experimental one including the prediction of the final fracture.

### Failure prediction of newly designed dog-bone tensile test

As shown in Figure 27(a), a newly designed dog-bone tensile specimen, which was not involved in any calibration procedures, is employed to validate the model and the calibrated parameters. The design is based on the same base dimension of dog-bone specimens. A different configuration of a circular cut with a notch radius of 30 mm is introduced at the centre of the gauge section. The minimum width of the specimen is accordingly 16.6 mm. The tensile experiment, coupled with the DCPD method, is carried out. The subsequent FE model of 1/8 of the specimen is constructed in ABAQUS/Explicit. The same mesh size is assigned at the critical zone of the specimen. The comparison of force–displacement responses is shown in Figure 27(b). An overall good agreement is achieved between the experimental and numerical results.

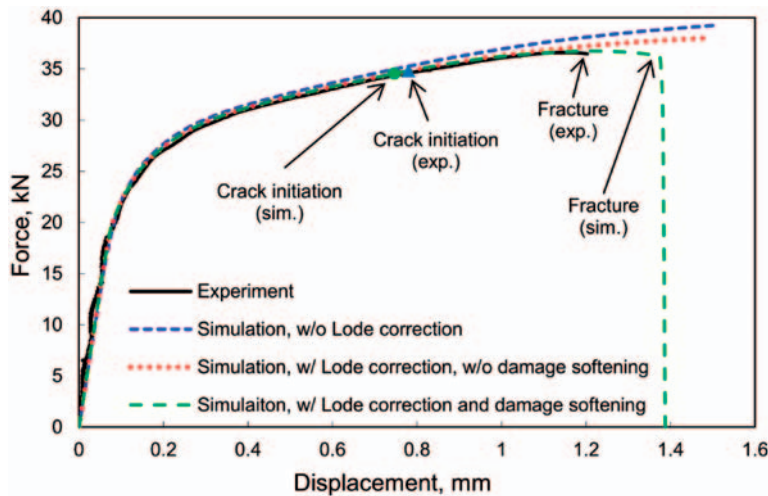


**Figure 25.** Validation of the model by comparison of the experimental and numerical load versus displacement curves for the plane strain specimen ( $R = 7.5$  mm).

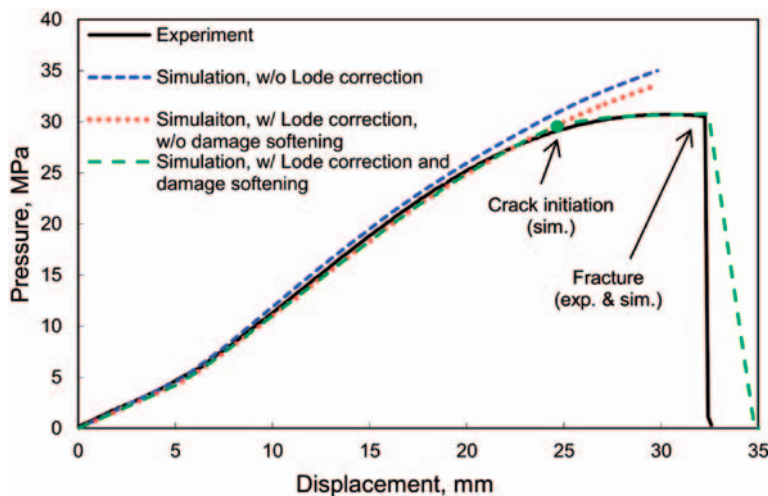


**Figure 26.** Validation of the model by comparison of the experimental and numerical load versus displacement curves for the bulge test.

## Discussion and conclusions

The onset of damage and the subsequent damage evolution have been key factors in the application of AHSS sheets due to the new ductile damage mechanisms in these modern high-strength steels. As a result, two demands are raised in the modelling of ductile damage: a microscopic criterion to indicate the onset of damage and a quantitative representation to express the extent of damage



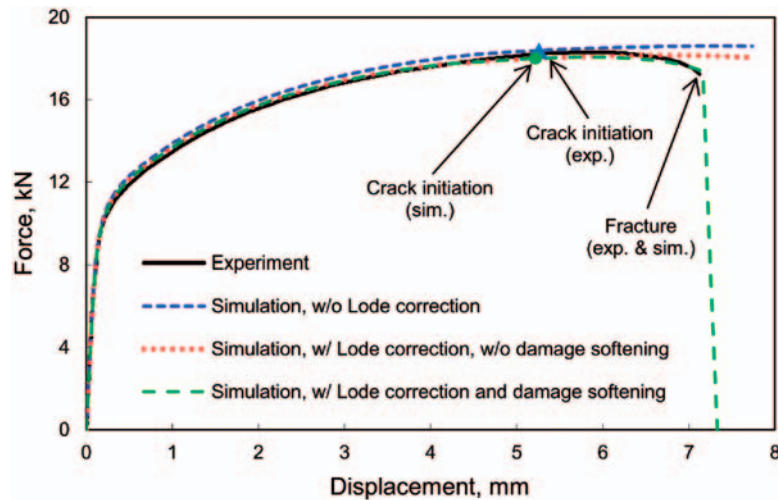


**Figure 27.** Validation of the model by comparison of the experimental and numerical load versus displacement curves for the newly designed dog-bone specimen ( $R = 30$  mm).

evolution. To meet these demands, a hybrid approach of ductile damage modelling is formulated in this study, which consists of three constituents originated from different damage models.

- Firstly, to achieve the great accuracy required for the damage modelling, a non-quadratic yield function which considers the Lode angle effect in conjunction with the associated flow rule and the isotropic hardening law is employed as the plasticity model. Under the assumption of isotropic materials, this model predicts the plastic behaviour of the chosen material with a relative error less than 2% for different loading conditions, while the conventional J2 plasticity gives the error between 2 and 5% at various stress states. The errors for both cases are calculated until the point of crack initiation. Though the former plasticity model gives more accurate prediction, for DP600 steel, the J2 plasticity also produces satisfactory results compared to for aluminium alloys (Bai and Wierzbicki, 2008; Gao et al., 2009b). However, the plasticity model here is only considered for the isotropic materials. Mohr et al. (2010) performed a study on the evaluation of the predictive capability of simple quadratic yield functions for multi-axial loading conditions with the consideration of material anisotropy for AHSS. From the comparison with experiments, the Hill (1948) quadratic anisotropic yield surface along with a non-associated flow rule also yields satisfactory results. To extend the current non-quadratic yield function to describe the material anisotropy behaviour besides the yielding difference and to compare the result with the quadratic forms are the ongoing research.
- Secondly, a phenomenological criterion which considers the influences of both the stress triaxiality and Lode angle is implemented and characterised to indicate the crack initiation. To express the effect of stress states, a wide range of stress states are realised by the design of different geometries of experimental tests. Tensile tests with central-hole, pure-shear and plane-strain specimens are introduced to calibrate the parameters for ductile crack initiation locus. To characterise the instant and location of microcrack initiation in the experiments, the DCPD method and SEM fractography are conducted. Compared to the relatively less pronounced influence of

the stress state on the stress–strain curve of DP600 steel sheets, a significant impact of the stress state on the ductile crack initiation locus is found.

- At last, a dissipation-energy-based damage evolution law is employed to quantitatively represent the microstructure degradation caused by damage-induced softening. The parameters are determined from the comparison of the force–displacement response of one dog-bone specimen. Though a good overall prediction of the fracture displacements is achieved by the current damage evolution law, a certain over-estimation is obtained in the plane-strain specimen. It can be traced to the function of the damage evolution law with respect to only the equivalent plastic strain rate. Research on the different formulation of the damage evolution law is an ongoing study.

The formulated model is numerically implemented into a user subroutine VUMAT in the commercial FE environment of ABAQUS/Explicit. Parameters in the three constituents are calibrated by a hybrid experimental/numerical approach. These calibrated parameters and the formation of the model are verified on different levels by experiments. These include the specimens partially involved in the calibration procedure and the specimen newly designed for the validation to correspond to different stress states. Good agreement between the experimental and numerical results in different stress states supports the validity of the formulation of the modelling framework and the calibrated parameters with the application of AHSS sheets.

### Funding

The authors also gratefully acknowledge the Deutsche Forschungsgemeinschaft (DFG) for providing the financial funding for the project ‘MU 2977/1-1’, which formed the basis for the investigations detailed in this paper.

### Acknowledgements

The authors are indebted to Prof Bleck (IEHK, Aachen) and Dr Sun (IWM, Freiburg) for inspiring and valuable discussions.

### References

- ABAQUS (2011) *User's Manual* (Version 6.11). Hibbit, Karlsson and Sorensen Inc.
- Atkins AG (1997) Fracture mechanics and metalforming: damage mechanics and the local approach of yesterday and today. In: Rossmannith HP (ed.) *Fracture Research in Retrospect, an Anniversary Volume in Honour of George R. Irwin's 90th Birthday*. Rotterdam: A.A. Balkema, pp.327–352.
- Bai YL and Wierzbicki T (2008) A new model of metal plasticity and fracture with pressure and Lode dependence. *International Journal of Plasticity* 24(6): 1071–1096.
- Bai YL and Wierzbicki T (2010) Application of extended Mohr-Coulomb criterion to ductile fracture. *International Journal of Fracture* 161(1): 1–20.
- Bao Y (2004) Dependence of fracture ductility on thickness. *Thin-Walled Structures* 42(8): 1211–1230.
- Bao Y and Wierzbicki T (2004a) A comparative study on various ductile crack formation criteria. *Journal of Engineering Materials and Technology* 126(3): 314.
- Bao Y and Wierzbicki T (2004b) On fracture locus in the equivalent strain and stress triaxiality space. *International Journal of Mechanical Sciences* 46(1): 81–98.
- Barlat F, Brem JC, Yoon JW, et al. (2003) Plane stress yield function for aluminum alloy sheets—part I: theory. *International Journal of Plasticity* 19(9): 1297–1319.
- Barsoum I and Faleskog J (2007) Rupture mechanisms in combined tension and shear—experiments. *International Journal of Solids and Structures* 44(6): 1768–1786.
- Besson J (2009) Continuum models of ductile fracture: a review. *International Journal of Damage Mechanics* 19(1): 3–52.

- Bonora N, Gentile D, Pirondi A, et al. (2005) Ductile damage evolution under triaxial state of stress: theory and experiments. *International Journal of Plasticity* 21(5): 981–1007.
- Brunig M, Chyra O, Albrecht D, et al. (2008) A ductile damage criterion at various stress triaxialities. *International Journal of Plasticity* 24(10): 1731–1755.
- Cazacu O (2004) A criterion for description of anisotropy and yield differential effects in pressure-insensitive metals. *International Journal of Plasticity* 20(11): 2027–2045.
- Cazacu O, Plunkett B and Barlat F (2006) Orthotropic yield criterion for hexagonal closed packed metals. *International Journal of Plasticity* 22(7): 1171–1194.
- Dunand M and Mohr D (2010) Hybrid experimental-numerical analysis of basic ductile fracture experiments for sheet metals. *International Journal of Solids and Structures* 47(9): 1130–1143.
- Dunand M and Mohr D (2011) On the predictive capabilities of the shear modified Gurson and the modified Mohr-Coulomb fracture models over a wide range of stress triaxialities and Lode angles. *Journal of the Mechanics and Physics of Solids* 59(7): 1374–1394.
- Gao X, Zhang G and Roe C (2009a) A study on the effect of the stress state on ductile fracture. *International Journal of Damage Mechanics* 19(1): 75–94.
- Gao X, Zhang T, Hayden M, et al. (2009b) Effects of the stress state on plasticity and ductile failure of an aluminum 5083 alloy. *International Journal of Plasticity* 25(12): 2366–2382.
- Gologanu M, Leblond JB and Devaux J (1993) Approximate models for ductile metals containing non-spherical voids—case of axisymmetrical prolate ellipsoidal cavities. *Journal of the Mechanics and Physics of Solids* 41(11): 1723–1754.
- Gologanu M, Leblond JB and Devaux J (1994) Approximate models for ductile metals containing non-spherical voids—case of axisymmetrical oblate ellipsoidal cavities. *Journal of Engineering Materials and Technology—Transactions of the ASME* 116(3): 290–297.
- Gologanu M, Leblond JB, Perrin G, et al. (1997) Recent extensions of Gurson's model for porous ductile metals. In: Suquet P (ed.) *Continuum Micromechanics, Cism Lectures Series*. New York: Springer-Verlag, pp.61–130.
- Gurson AL (1977) Continuum theory of ductile rupture by void nucleation and growth: part I—yield criteria and flow rules for porous ductile media. *Journal of Engineering Materials and Technology—Transactions of the ASME* 99(1): 2–15.
- Hancock JW and Brown DK (1983) On the role of strain and stress state in ductile failure. *Journal of the Mechanics and Physics of Solids* 31(1): 1–24.
- Hancock JW and Mackenzie AC (1976) Mechanisms of ductile failure in high-strength steels subjected to multi-axial stress states. *Journal of the Mechanics and Physics of Solids* 24(2–3): 147–160.
- Hershey AV (1954) Plasticity of isotropic aggregate of anisotropic facecentered cubic crystals. *Journal of Applied Mechanics* 21: 241–249.
- Hill R (1948) A theory of the yielding and plastic flow of anisotropic metals. *Proceedings of the Royal Society of London, Series A* 193(1033): 281–297.
- Hosford WF (1972) A generalized isotropic yield criterion. *Journal of Applied Mechanics* 39(2): 607–609.
- Hu WL and Wang ZR (2005) Multiple-factor dependence of the yielding behavior to isotropic ductile materials. *Computational Materials Science* 32(1): 31–46.
- Jiang J and Pietruszczak S (1988) Convexity of yield loci for pressure sensitive materials. *Computers and Geotechnics* 5(1): 51–63.
- Johnson GR and Cook WH (1985) Fracture characteristics of 3 metals subjected to various strains, strain rates, temperatures and pressures. *Engineering Fracture Mechanics* 21(1): 31–48.
- Kachanov LM (1999) Rupture time under creep conditions. *International Journal of Fracture* 97(1–4): xi–xviii.
- Kailasam M and Castaneda PP (1998) A general constitutive theory for linear and nonlinear particulate media with microstructure evolution. *Journal of the Mechanics and Physics of Solids* 46(3): 427–465.
- Lemaitre J (1985) A continuous damage mechanics model for ductile fracture. *Journal of Engineering Materials and Technology—Transactions of the ASME* 107(1): 83–89.
- Lemaitre J (1992) *A Course on Damage Mechanics*. Berlin: Springer-Verlag.



- Li H, Fu MW, Lu J, et al. (2011) Ductile fracture: experiments and computations. *International Journal of Plasticity* 27(2): 147–180.
- Mackenzie AC, Hancock JW and Brown DK (1977) Influence of state of stress on ductile failure initiation in high-strength steels. *Engineering Fracture Mechanics* 9(1): 167–188.
- McClintock FA (1968) A criterion for ductile fracture by growth of holes. *Journal of Applied Mechanics* 35(2): 363–371.
- Mirone G (2004) A new model for the elastoplastic characterization and the stress–strain determination on the necking section of a tensile specimen. *International Journal of Solids and Structures* 41(13): 3545–3564.
- Mirone G and Corallo D (2010) A local viewpoint for evaluating the influence of stress triaxiality and Lode angle on ductile failure and hardening. *International Journal of Plasticity* 26(3): 348–371.
- Mirza MS, Barton DC and Church P (1996) The effect of stress triaxiality and strain-rate on the fracture characteristics of ductile metals. *Journal of Materials Science* 31(2): 453–461.
- Mohr D, Dunand M and Kim K-H (2010) Evaluation of associated and non-associated quadratic plasticity models for advanced high strength steel sheets under multi-axial loading. *International Journal of Plasticity* 26(7): 939–956.
- Münstermann S (2006) *Numerische Beschreibung Des Duktilen Versagensverhaltens Von Hochfesten Baustählen Unter Berücksichtigung Der Mikrostruktur*. PhD dissertation. RWTH-Aachen University.
- Münstermann S, Uthaisangsuk V, Pahl U, et al. (2007) Experimental and numerical failure criteria for sheet metal forming. *Steel Research International* 78(10–11): 762–770.
- Nahshon K and Hutchinson JW (2008) Modification of the Gurson model for shear failure. *European Journal of Mechanics A-Solids* 27(1): 1–17.
- Nielsen KL and Tvergaard V (2009) Effect of a shear modified Gurson model on damage development in a Fsw tensile specimen. *International Journal of Solids and Structures* 46(3–4): 587–601.
- Nielsen KL and Tvergaard V (2010) Ductile shear failure or plug failure of spot welds modelled by modified Gurson model. *Engineering Fracture Mechanics* 77(7): 1031–1047.
- Racherla V and Bassani JL (2007) Strain burst phenomena in the necking of a sheet that deforms by non-associated plastic flow. *Modelling and Simulation in Materials Science and Engineering* 15(1): S297–S311.
- Rice JR and Tracey DM (1969) On ductile enlargement of voids in triaxial stress fields. *Journal of the Mechanics and Physics of Solids* 17(3): 201–217.
- Schlüter N, Grimpe F, Bleck W, et al. (1996) Modelling of the damage in ductile steels. *Computational Materials Science* 7(1–2): 27–33.
- Tasan CC, Hoefnagels JPM, ten Horn CHLJ, et al. (2009) Experimental analysis of strain path dependent ductile damage mechanics and forming limits. *Mechanics of Materials* 41(11): 1264–1276.
- Teng X (2008) Numerical prediction of slant fracture with continuum damage mechanics. *Engineering Fracture Mechanics* 75(8): 2020–2041.
- Tvergaard V (1981) Influence of voids on shear band instabilities under plane-strain conditions. *International Journal of Fracture* 17(4): 389–407.
- Tvergaard V (1982) On localization in ductile materials containing spherical voids. *International Journal of Fracture* 18(4): 237–252.
- Tvergaard V and Needleman A (1984) Analysis of the cup-cone fracture in a round tensile bar. *Acta Metallurgica* 32(1): 157–169.
- Uthaisangsuk V (2009) *Microstructure Based Formability Modelling of Multiphase Steels*. PhD dissertation. RWTH-Aachen University.
- Xue L (2008) Constitutive modeling of void shearing effect in ductile fracture of porous materials. *Engineering Fracture Mechanics* 75(11): 3343–3366.